Wind channeling, magnetospheres, and spindown of magnetic massive stars

S. P. Owocki[1], A. ud-Doula[2], R. H. D. Townsend[3], V. Petit[1], J. O. Sundqvist[4] and D. H. Cohen[5]

[1]Department of Physics & Astronomy, University of Delaware, Newark, DE 19716 USA
email: `owocki@udel.edu`

[2]Penn State Worthington Scranton, Dunmore, PA, USA

[3]Dept. of Astronomy, University of Wisconsin-Madison, Madison, WI, USA

[4]Universitaetssternwarte Muenchen, Scheinerstr. 1, 81679 Muenchen, Germany

[5]Dept. of Physics & Astronomy, Swarthmore College, Swarthmore, PA, USA

Abstract. A subpopulation ($\sim 10\%$) of hot, luminous, massive stars have been revealed through spectropolarimetry to harbor strong (hundreds to tens of thousand Gauss), steady, large-scale (often significantly dipolar) magnetic fields. This review focuses on the role of such fields in channeling and trapping the radiatively driven wind of massive stars, including both in the strongly perturbed outflow from open field regions, and the wind-fed "magnetospheres" that develop from closed magnetic loops. For B-type stars with weak winds and moderately fast rotation, one finds "centrifugal magnetospheres", in which rotational support allows magnetically trapped wind to accumulate to a large density, with quite distinctive observational signatures, e.g. in Balmer line emission. In contrast, more luminous O-type stars have generally been spun down by magnetic braking from angular momentum loss in their much stronger winds. The lack of centrifugal support means their closed loops form a "dynamical magnetosphere", with trapped material falling back to the star on a dynamical timescale; nonetheless, the much stronger wind feeding leads to a circumstellar density that is still high enough to give substantial Balmer emission. Overall, this review describes MHD simulations and semi-analytic dynamical methods for modeling the magnetospheres, the magnetically channeled wind outflows, and the associated spin-down of these magnetic massive stars.

Keywords. Stars – early-type, Stars – magnetic fields, Stars – mass loss, Stars – X-rays, Stars – Rotation

1. Introduction

Massive, luminous, hot stars lack the hydrogen recombination convection zone that induces the magnetic dynamo cycle of cooler, solar-type stars. Nonetheless, modern spectropolarimetry has revealed that about 10% of O, B and A-type stars harbor large-scale, organized (often predominantly dipolar) magnetic fields ranging in dipolar strength from a few hundred to tens of thousand Gauss. (See contribution by G. Wade in these proceedings). Petit *et al.* (2013) recently compiled an exhaustive list of 64 confirmed magnetic OB stars with $T_{\rm eff} \gtrsim 16\,{\rm kK}$, along with their physical, rotational and magnetic properties; see figure **??** below.

The review here summarizes efforts to develop dynamical models for the effects of such large-scale surface fields on the radiatively driven mass outflow from such OB stars. The focus is on the properties and observational signatures (e.g. in X-ray and Balmer line emission) of the resulting wind-fed *magnetospheres* in closed loop regions, and on the
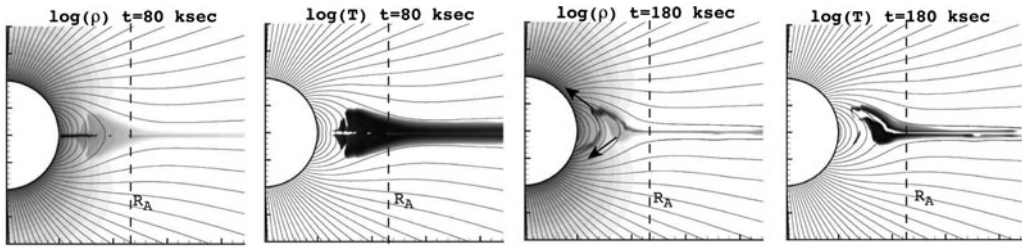
Figure 1. 2D MHD simulation for magnetic channeling and confinement of radiatively driven stellar wind from a non-rotating hot-star with $\eta_* = 15$ (and so $R_A \approx 2.3R_*$), showing the logarithm of density ρ and temperature T in a meridional plane. At a time 80 ksecs after the initial condition, the magnetic field has channeled wind material into a compressed, hot region about the magnetic equator, much as envisioned in the Magnetically Confined Wind Shock (MCWS) paradigm of Babel & Montmerle (1997a,b). But by a time of 180 ksecs, the cooled equatorial material is falling back toward the star along field lines, in a complex 'snake' pattern. The darkest areas of the temperature plots represent gas at $T \sim 10^7$ K, hot enough to produce relatively hard X-ray emission of a few keV. The model reproduces quite well the observed X-ray properties of θ^1 Ori C (Gagné *et al.* 2005).

stellar rotation *spindown* that results from the angular momentum loss associated with magnetically torqued wind outflow from open field regions.

## 2. MHD of Wind Outflows from Magnetic Hot Stars

2.1. *Wind magnetic confinement parameter and Alfvén radius*

MHD simulation studies (e.g. ud-Doula & Owocki 2002; ud-Doula *et al.* 2008) show that the overall net effect of a large-scale, dipole magnetic field in diverting such a hot-star wind can be well characterized by a single *wind magnetic confinement parameter* and its associated *Alfvén radius*,

$$\eta_* \equiv \frac{B_{eq}^2\, R_*^2}{\dot{M}\, v_\infty} \quad ; \quad \frac{R_A}{R_*} \approx 0.3 + (\eta_* + 0.25)^{1/4} \;, \tag{2.1}$$

where $B_{\mathrm{eq}} = B_{\mathrm{p}}/2$ is the field strength at the magnetic equatorial surface radius R_*, and $\dot{M}$ and v_∞ are the fiducial mass-loss rate and terminal speed that the star *would have* in the *absence* of any magnetic field. This confinement parameter sets the scaling for the ratio of the magnetic to wind kinetic energy density. For a dipole field, the r^{-6} radial decline of magnetic energy density is much steeper than the r^{-2} decline of the wind's mass and energy density; this means the wind always dominates beyond the Alfvén radius, which scales as $R_A \sim \eta_*^{1/4}$ in the limit $\eta_* \gg 1$ of strong confinement.

As shown in figure 1, magnetic loops extending above R_A are drawn open by the wind, while those with an apex below R_A remain closed. Indeed, the trapping of wind upflow from opposite footpoints of closed magnetic loops leads to strong collisions that form X-ray emitting, *magnetically confined wind shocks* (MCWS; Babel & Montmerle 1997a,b). The post-shock temperatures $T \approx 20$ MK are sufficient to produce the moderately hard (~ 2 keV) X-rays observed in the prototypical magnetic O-star θ^1 Ori C (Gagné *et al.* 2005). As illustrated by the downward arrows in the density plot at a simulation time $t = 180$ ksec, once this material cools back to near the stellar effective temperature, the high-density trapped material falls back onto the star over a dynamical timescale.
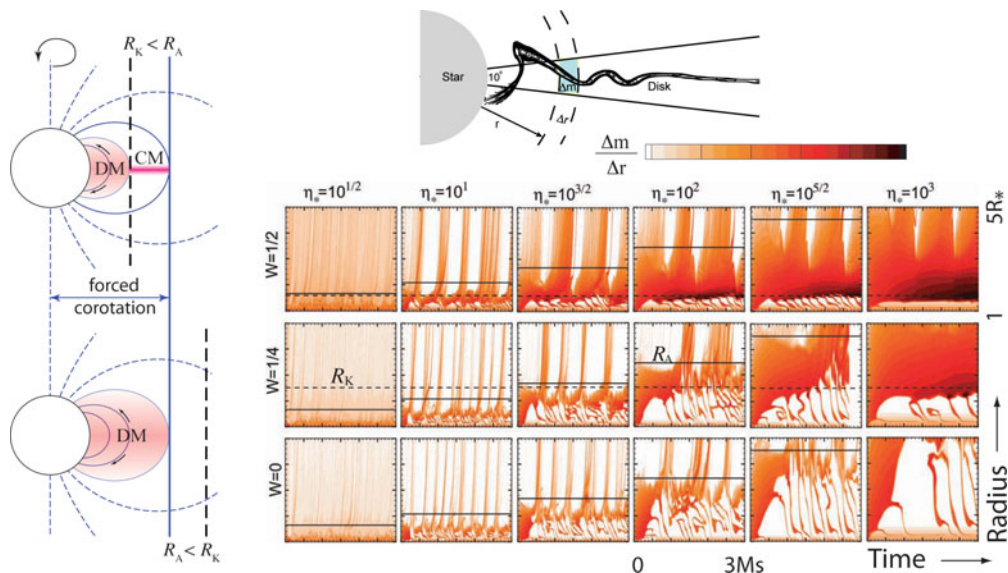
Figure 2. *Left:* Sketch of the regimes for a dynamical vs. centrifugal magnetosphere (DM vs. CM). The lower panel illustrates the case of a slowly rotating star with Kepler radius beyond the Alfvén radius ($R_\mathrm{K} > R_\mathrm{A}$); the lack of centrifugal support means that trapped material falls back to the star on a dynamical timescale, forming a DM, with shading illustrating the time-averaged distribution of density. The upper panel is for more rapid rotation with $R_\mathrm{K} < R_\mathrm{A}$, leading then to a region between these radii where a net outward centrifugal force against gravity is balanced by the magnetic tension of closed loops; this allows material to build up to the much higher density of CM. *Right, Upper:* Contour plot for density at arbitrary snapshot of an isothermal 2D MHD simulation with magnetic confinement parameter $\eta_* = 100$ and critical rotation factor $W = 1/2$. The overlay illustrates the definition of radial mass distribution, $\Delta m/\Delta r$, within $10°$ of the equator. *Right, Lower:* Densityplots for log of $\Delta m/\Delta r$, plotted versus radius (1-5 R_*) and time (0-3 Msec), for a mosaic of 2D MHD models with a wide range of magnetic confinement parameters η_*, and 3 orbital rotation fractions W. The horizontal solid lines indicate the Alfvén radius R_A (solid) and the horizontal dashed lines show Kepler radius R_K (dashed).

2.2. *Orbital rotation fraction and Kepler co-rotation radius*

The dynamical effects of rotation can be analogously parameterized (ud-Doula *et al.* 2008) in terms of the *orbital rotation fraction*, and its associated *Kepler corotation radius*,

$$W \equiv \frac{V_\mathrm{rot}}{V_\mathrm{orb}} = \frac{V_\mathrm{rot}}{\sqrt{GM_*/R_*}} \quad ; \quad R_\mathrm{K} = W^{-2/3} R_* \tag{2.2}$$

which depend on the ratio of the star's equatorial rotation speed to the speed to reach orbit near the equatorial surface radius R_*. Insofar as the field within the Alfvén radius is strong enough to maintain *rigid-body rotation*, the Kepler corotation radius R_K identifies where the centrifugal force for rigid-body body rotation exactly balances the gravity in the equatorial plane. If $R_\mathrm{A} < R_\mathrm{K}$, then material trapped in closed loops will again eventually fall back to the surface, forming a *dynamical magnetosphere* (DM). But if $R_\mathrm{A} > R_\mathrm{K}$, then wind material located between R_K and R_A can remain in static equilibrium, forming a *centrifugal magnetosphere* (CM) that is supported against gravity by the magnetically enforced rotation. As illustrated in the upper left schematic in figure 2, the much longer confinement time allows material in this CM region to build up to a much higher density than in a DM region.
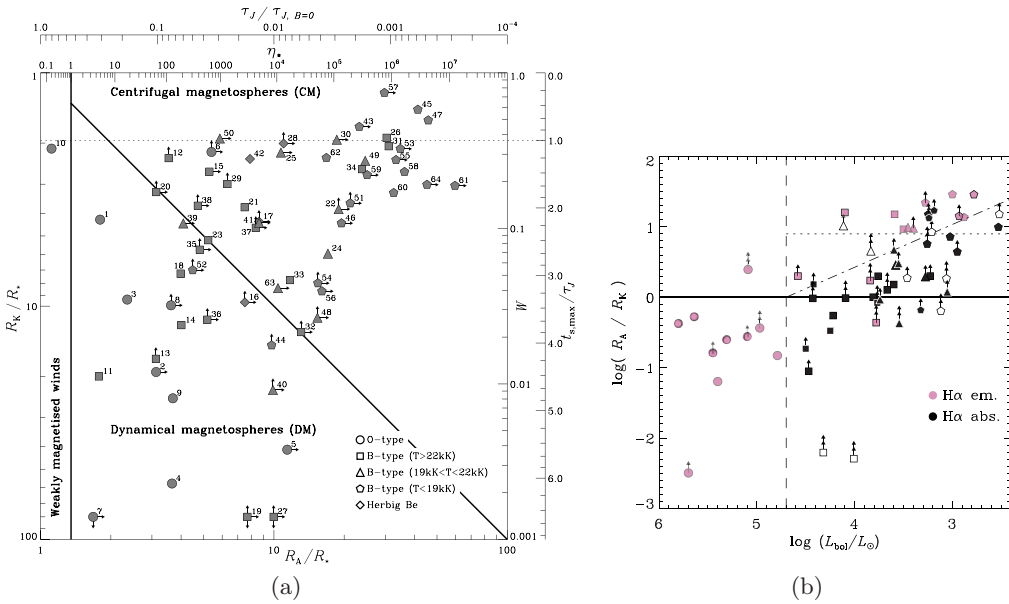
Figure 3. (a.) Classification of 64 observationally confirmed magnetic massive stars in terms of magnetic confinement vs. rotation fraction, characterized here by a log-log plot of Kepler radius R_K increasing downward vs. Alfvén radius R_A increasing to the right. The labeled ID numbers are sorted in order of decreasing T_{eff}, with stellar identities given in Table 1 of Petit *et al.* (2013). The solid lines separate the magnetosphere domains of weakly magnetized winds (with $\eta_* < 1$), dynamical magnetospheres (DM) with $R_A < R_K$, and centrifugal magnetospheres (CM) with $R_A > R_K$. The additional upper and right axes give respectively the corresponding spindown timescale τ_J, and maximum spindown age $t_{s,\text{max}}$, as defined in §3.4. Rapidly rotating stars above the horizontal dotted line have a maximum spindown age $t_{s,\text{max}}$ that is less than one spindown time τ_J. (b.) Location of magnetic massive stars in a log-log plot of R_A/R_K vs. stellar luminosity. The symbol shadings mark the presence (pink or shaded) or absence (black) of magnetospheric Hα emission, with empty symbols when no Hα information is available. The vertical dashed line represents the luminosity transition between O-type and B-type main sequence stars. The horizontal dotted line and the diagonal dot-dashed line show division of the CM domain according to potential magnetospheric leakage mechanisms.

For full 2D MHD simulations in the axisymmetric case of a rotation-axis aligned dipole, the mosaic of color plots in figure 2 shows the time vs. height variation of the equatorial mass distribution $\Delta m/\Delta r$ for various combinations of rotation fraction W and wind confinement η_* that respectively increase upward and to the right. This illustrates vividly the DM infall for material trapped below R_K and R_A, vs. the dense accumulation of a CM from confined material near and above R_K, but below R_A.

3. Comparison with Observations of Confirmed Magnetic Hot-stars

For the 64 observationally confirmed magnetic hot-stars ($T_{\text{eff}} \gtrsim 16\,\text{kK}$) compiled by Petit *et al.* (2013), figure **??** plots positions in a log-log plane of R_K vs. R_A. The vertical solid line representing $\eta_* = 1$ separates the domain of non-magnetized or weakly magnetized winds to left, from the domain of stellar magnetospheres to the right. The diagonal line representing $R_K = R_A$ divides the domain of centrifugal magnetospheres (CM) to the upper right from that for dynamical magnetospheres (DM) to the lower left. Let us now consider how these distinctions in magnetospheric properties organize their observational characteristics.
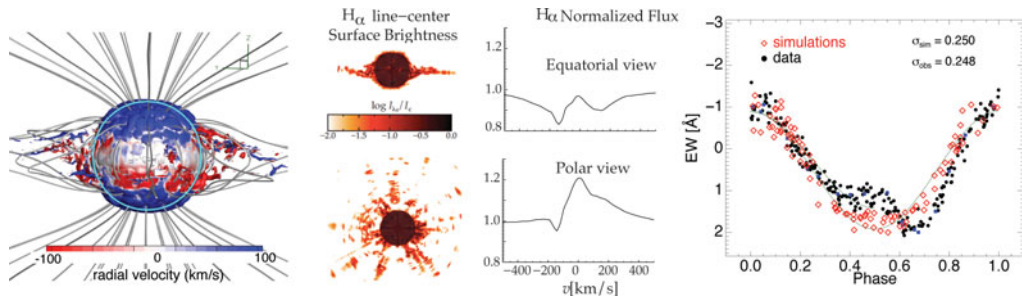
Figure 4. 3D MHD model of the dynamical magnetosphere for the young, slowly rotating (15.4-day period) O7V star θ^1 Ori C (ud-Doula *et al.* 2012). The left panel shows a snapshot of wind structure drawn as isodensity surface, colored to show radial component of velocity. The middle panels shows the predicted equatorial and polar views of Hα line-center surface brightness, along with corresponding line-flux profiles. The right panel compares the observed rotational modulation of the Hα equivalent width (black) with 3D model predictions (red) assuming a pure-dipole surface field tilted by $\beta = 45°$ to the rotation axis, as viewed from the inferred observer inclination of $i = 45°$.

3.1. *Balmer-α line emission from DM and CM*

Figure 3(b) plots these observed magnetic stars in a diagram comparing the *ratio* $R_{\rm A}/R_{\rm K}$ vs. stellar luminosity, with now the symbol coded to mark the presence (light shading) or absence (black) of magnetospheric Hα emission. The horizontal solid line marks the transition between the CM domain above and the DM domain below, while the vertical dashed line marks the divide between O- and B-type main sequence stars. Note that *all* O-stars show emission, with all but one (Plaskett's star, which has likely been spun-up by mass exchange from its close binary companion; Grunhut *et al.* 2013) located among the slow rotators with a DM. By contrast, most B-type stars only show emission if they are well above the $R_{\rm A}/R_{\rm K} = 1$ horizontal line, implying a relatively fast rotation and strong confinement that leads to a CM.

The basic explanation for this dichotomy is straightforward. The stronger winds driven by the higher luminosity O-stars can accumulate even within a relatively short dynamical timescale to a sufficient density to give the strong emission in a DM, while the weaker winds of lower luminosity B-stars require the longer confinement and buildup of a CM to reach densities for such emission. This general picture is confirmed by the detailed dynamical models of DM and CM emission that motivated this empirical classification.

For the slowly rotating O-stars HD 191612 and θ^1 Ori C (here with respective ID numbers 4 and 3), both 2D and 3D MHD simulations (Sundqvist *et al.* 2012; ud-Doula *et al.* 2012) of the wind-fed DM reproduce quite well the rotational variation of Hα emission. For the 3D simulations of θ^1 Ori C, figure 4 shows how wind material trapped in closed loops over the magnetic equator (left panel) leads to circumstellar emission that is strongest during rotational phases corresponding to pole-on views (middle panel). For a pure dipole with the inferred magnetic tilt $\beta = 45°$, an observer with the inferred inclination $i = 45°$ has perspectives that vary from magnetic pole to equator, leading in the 3D model to the rotational phase variations in Hα equivalent width shown in the right panel (shaded circles). This matches quite well both the modulation and random fluctuation of the observed equivalent width (black dots), though accounting for the asymmetry about minimum will require future, more detailed models that include a secondary, higher-order (non-dipole) component of the inferred surface field.
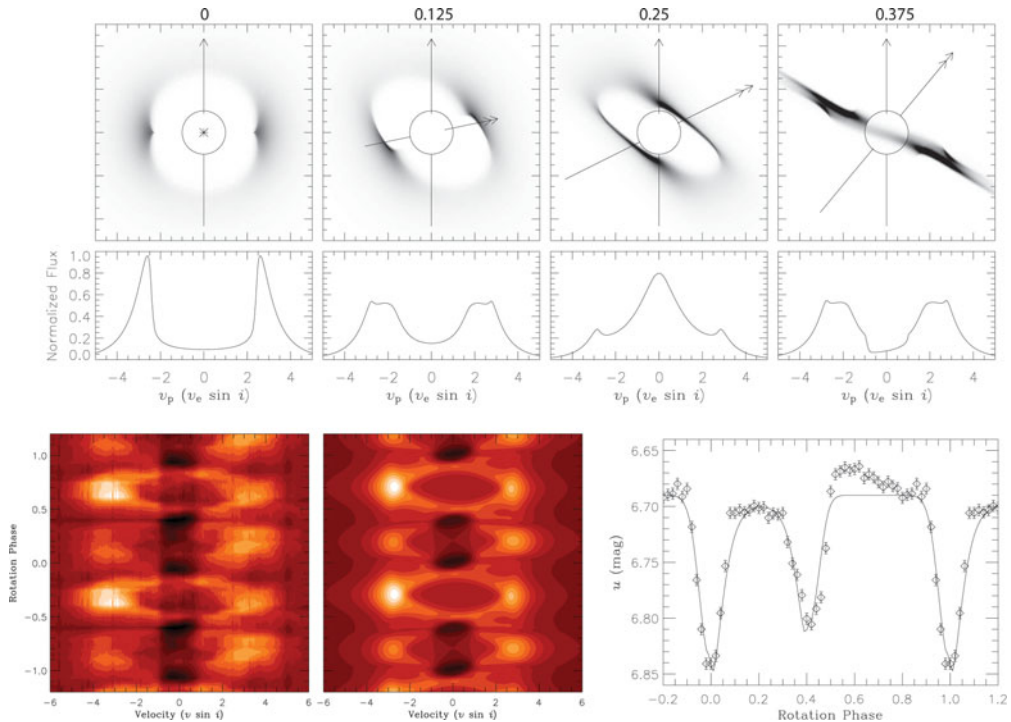
Figure 5. Observational signatures of the CM in the moderately fast rotator (1.2-day period) B2V star σ Ori E, compared with results from the RRM model (Townsend and Owocki 2005). The top row shows surface maps of Hα emission and resulting emission line profiles at the marked rotational phases. The lower-row density plots are associated dynamic Hα spectra, showing the variations relative to the photospheric profile over two rotation periods of $\sim 1.2d$; white indicates emission, and black absorption. The left panel is based on echelle observations of the star, while the right panel is the prediction from the RRM model. The lower-right line plot shows the Strömgren u-band light curve of σ Ori E, revealing the eclipse-like dimmings that occur when its two magnetospheric clouds transit in front of the star. The solid line indicates the predictions of an early RRM model.

3.2. *The Rigidly Rotating Magnetosphere (RRM) model*

In modeling the CM of more rapidly rotating, strongly magnetic B-stars like σ Ori E, a key challenge stems from the fact that their wind magnetic confinement parameters are generally of order $\eta_* \sim 10^6$ or more, far beyond the maximum $\eta_* \approx 10^3$ achieved with direct MHD simulations, which are limited by the Courant stability criterion. As an alternative for this *strong-field limit*, Townsend & Owocki (2005) developed a *Rigidly Rotating Magnetosphere* (RRM) model that uses a semi-analytical prescription for the 3D magnetospheric plasma distribution, based on the form and minima of the total gravitational-plus-centrifugal potential along each separate field line. Townsend *et al.* (2005) applied this RRM model to synthesize the emission from material trapped in the associated CM of σ Ori E. Figure 5 compares the predicted variation of the dynamic emission spectrum over the 1.2 day rotational period with that obtained from echelle observations of the star. The agreement is again very good, providing strong general support for this RRM model for Hα emission from the CM of σ Ori E.

The basic RRM concept has been further developed in a successor *Rigid Field Hydrodynamics* (RFHD) model (Townsend *et al.* 2007), wherein the time-dependent flow along each individual field line is simulated using a 1D hydro code. By piecing together
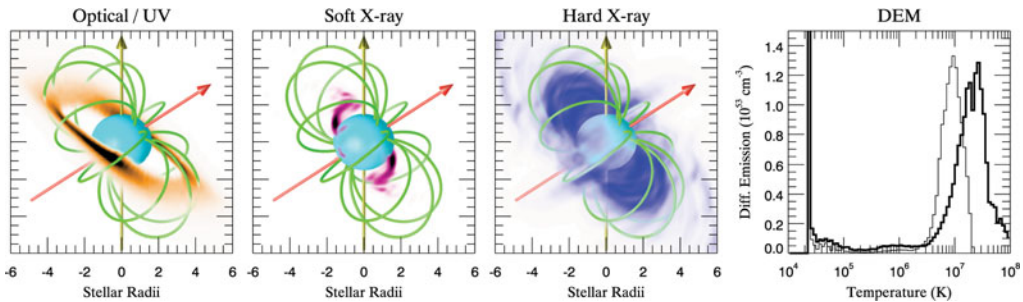
Figure 6. Snapshots from an RFHD model of σ Ori E, showing the spatial distribution of magnetospheric emission measure in three different temperature bins: optical ($T < 10^6$ K), soft X-ray (10^6 K $< T < 10^7$ K) and hard X-ray ($T > 10^7$ K). The plot on the right shows the corresponding differential emission measure, for models with (thin) and without (thick) thermal conduction.
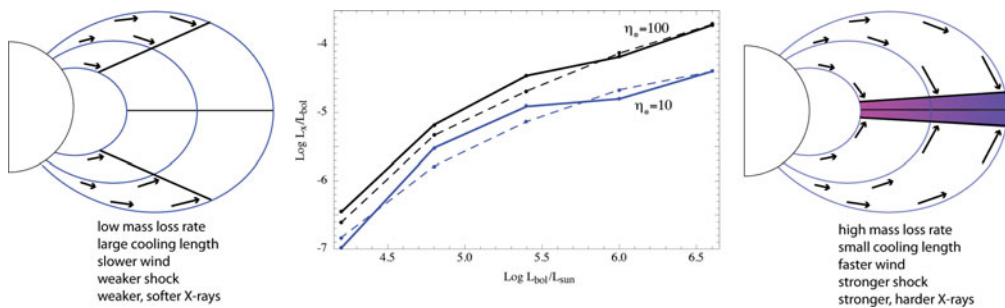
Figure 7. Scaling of X-ray luminosities L_x (for energies $E_x > 0.3$ keV) with stellar bolometric luminosity L_{bol} (center), for X-ray simulations with (solid) and without (dashed) inverse Compton cooling (from ud-Doula *et al.*, in prep). The left and right schematics illustrate the effect of "shock retreat" in reducing the strength and hardness of X-rays in lower luminosity stars with lower mass loss rate and thus less efficient radiative cooling.

independent simulations of many different field lines (typically, several *thousand*!), a 3D picture of a star's magnetosphere can be constructed at modest computational cost, leading in turn to predictions for not only Hα but also for X-ray emission (and other wind-related observables) of magnetospheres in the strong-field limit, as shown figure 6. A powerful aspect of both the RRM and RFHD models is that, within the strong field limit, they are in principle applicable to arbitrary field topologies, not just the oblique dipole configurations considered so far. Thus, for example, they could be used to model the magnetosphere of HD 37776, which harbors high-order multipoles (Kochukhov *et al.* 2011).

3.3. *MHD scalings for X-ray luminosity from MCWS*

A recent focus of MHD simulation parameter studies has been to derive predicted scaling relations for the X-ray luminosity L_x that results from magnetically confined wind shocks (MCWS). The central panel of figure 7 plots the ratio L_x/L_{bol} vs. the bolometric luminosity L_{bol} for models with magnetic confinement $\eta_* = 10$ and 100. The dashed curves assume the post-shock cooling is purely by radiative emission, while the solid curves account also for the effects of inverse Compton cooling. For the most luminous stars, L_x scales in proportion to the wind mass loss rate, which for line-driven winds follows $\dot{M} \sim L_{bol}^{1.6}$; but at lower L_{bol}, the lower $\dot{M}$ means the radiative cooling becomes inefficient. As illustrated in the left vs. right schematic panels, the larger cooling layer

forces a "shock retreat" back to lower, slower wind outflow, leading to weaker shocks, and so lower, softer X-ray emission. But overall the X-ray luminosity from this MWCS mechanism is predicted to be well above the canonical $L_x \sim 10^{-7} L_{bol}$ inferred for non-magnetic O-type stars (Chlebowski *et al.* 1989). Work is underway to compare these theoretical predictions with scalings of observed X-ray properties of magnetic massive stars. (See the proceedings contribution by V. Petit.)

3.4. *Magnetic wind braking, spindown time, and spindown age*

Let us now turn to the issue of rotational spindown from magnetic wind braking. In this regard, the case of σ Ori E provides a key testbed, because extended photometric monitoring of the timing of magnetospheric clouds transiting in front of the star (Townsend *et al.* 2008; see also lower right panel of figure 5) has allowed a *direct* measurement of the change in rotation period, yielding a spindown time of 1.34 Myr (Townsend *et al.* 2010). This is remarkably close to the spindown time *predicted* previously by ud-Doula *et al.* (2009), based on the same 2D MHD aligned-dipole parameter study used for figure 2.

This MHD study showed that the angular momentum carried out by a magnetically torqued stellar wind follows the same simple, split-monopole scaling law derived for the Sun by Weber and Davis (1967), $\dot{J} = \frac{2}{3}\dot{M}\Omega R_A^2$ – with, however, the Alfvén radius R_A now given by the *dipole* scaling $R_A \sim \eta_*^{1/4}$, instead the oft-quoted, stronger scaling ($R_A \sim \eta_*^{1/2}$) for a split monopole. This leads to an associated general formula for the rotational braking timescale,

$$\tau_J \equiv \frac{I\Omega}{\dot{J}} = \frac{3}{2}f\tau_{\text{mass}}\left(\frac{R_*}{R_A}\right)^2 \approx 0.15\frac{\tau_{\text{mass}}}{\sqrt{\eta_*}}. \qquad (3.1)$$

Here $\tau_{\text{mass}} \equiv M/\dot{M}$ is the stellar mass loss timescale, and $f \approx 0.1$ is a dimensionless measure of the star's moment of inertia $I \equiv fMR_*^2$.

If we assume for simplicity a fixed radius R_* and moment of inertia factor $f \approx 0.1$, as well as a constant angular momentum loss rate $\dot{J}$, then the stellar rotation period P will simply increase exponentially with age t from its initial value, $P(t) = P_o e^{t/\tau_J}$. This can be used to define a star's spindown *age*, t_s, in terms of the spindown time τ_J, and its inferred present-day critical rotation fraction $W = P_{\text{orb}}/P$ relative to its initial rotation fraction W_o, $t_s = \tau_J(\ln W_o - \ln W)$. Taking the initial rotation to be critical, $W_o = 1$, yields a simple upper limit to the spindown age,

$$t_{s,\text{max}} = \tau_J \, \ln(1/W). \qquad (3.2)$$

If the initial rotation is subcritical, $W_o < 1$, then the actual spindown age is shorter by a time $\Delta t_s = \tau_J \ln W_o$.

In figure 3(a) the upper axis gives the spindown timescale τ_J (normalized by the value in a non-magnetized wind), while the right axis gives the maximum spindown age $t_{s,\text{max}}$ (normalized by the spindown time). Stars above the horizontal dotted line have a maximum spindown age that is *less* than a single spindown time. Together with the R_A/R_K vs. luminosity plot in figure 3(b), we can identify some important features and trends:

• All the most rapidly rotating stars are cooler B-type with weak winds, and thus weak braking, despite their strong field. The two most extreme examples (ID 45 and 47) may be very close to critical rotation, and so provide a potential link to Be stars, which have *not* been found to have strong ordered fields, but for which rapid rotation is linked to decretion into an orbiting Keplerian disk.

• The only rapidly rotating O-star is Plaskett's star (ID 6), which has likely been spun up by mass exchange with its close binary companion (Grunhut *et al.* 2013). Many O-

stars have very long rotation period, e.g. 538 days for the field star HD 191612 (ID 4), suggesting substantial main-sequence spindown by wind magnetic braking, with a spindown age comparable to its estimated main-sequence age.

• In contrast, the young Orion cluster star θ^1 Ori C (ID 3) has a moderately slow (15.4-day period) rotation, but is generally thought to be about 1 Myr old (Hillenbrand 1997; Scandariato *et al.* 2012), much less than its maximum spindown age $t_{s,max} \approx 3\tau_J \approx$ 10 Myr. Thus its ZAMS rotation was likely already quite slow, suggesting significant *pre-main-sequence* braking, e.g. by PMS disk-locking, or through a PMS jet and/or wind. (See review by Pudritz in these proceedings.)

To reinforce the last point, the recent survey of Herbig Ae/Be stars by Alecian *et al.* (2013a,b) concludes that magnetic HeAeBe stars have a slower rotation than those without a detected field. Among their sample of non-magnetic stars they further find that those with lower mass evolve toward the ZAMS with a constant angular momentum, whereas higher mass ($> 5M_\odot$) stars show evidence of angular momentum loss during their PMS evolution, most likely as a result of their stronger, radiatively driven mass loss.

4. Future Outlook

The above shows there has been substantial progress in our efforts to understand the physical and observational properties of massive-star magnetospheres. But there are still important gaps in this understanding and key limitations to the physical realism of the models developed. The following lists some specific areas for future work:

• *3D MHD of Non-Axisymmetric Cases:* Thus far all MHD simulations, whether run in 2D or 3D, have been restricted to cases with an underlying axial symmetry, assuming a purely dipole field either without dynamically significant rotation, or with rotation that is taken to be aligned with the magnetic dipole axis. Fully 3D simulations are needed for both the many stars with an oblique dipole, as well as cases with more complex, higher-order multi-pole fields.

• *Spindown from oblique dipoles or higher-order multipoles:* An important application of these 3D MHD models will be to analyze the angular momentum loss from oblique dipole fields, as well as from higher-order fields. This will allow determination of generalized spindown scalings for complex fields, and provide the basis for interpreting anticipated future direct measurements of magnetic braking in stars with tilted-dipole or higher multi-pole fields.

• *Non-Ideal MHD and magnetospheric leakage:* In MHD simulations of slowly rotating magnetic stars with a DM, the dynamical infall of material back to the star balances the mass feeding from the stellar wind, yielding an overall mass and density that is in quite good agreement with absorption and emission diagnostics. By contrast, in CM simulations the much longer confinement and mass buildup is limited only by eventual centrifugal breakout of regions beyond the Kepler radius (Townsend & Owocki 2005), and this now leads to an overall predicted CM mass and density that significantly exceeds values inferred by observational diagnostics. To understand better the mass budget of CM's, it will be necessary to investigate additional plasma leakage mechanisms, such as the field line interchange transport that is thought to be key to mass balance of planetary magnetospheres (Kivelson & Southwood 2005). In addition to comparison with emission diagnostics of individual stars, this should aim to derive general scaling laws that can explain the trends for Balmer emission seen in Figure 3(b), particularly the boundary between Hα emission and absorption in B-type stars.

- *Rapid rotation and gravity darkening:* To model the rapidly rotating magnetic B-stars with $W = V_{rot}/V_{orb} > 1/2$, there is a need to generalize the lower boundary condition for both MHD and RFHD models to account for stellar oblateness, while also including the effect of gravity darkening for the wind radiative driving. This will also allow a link to Be stars, to constrain upper limits on the dynamical role of (undetected) magnetic fields in their quite distinctively Keplerian (vs. rigid-body) decretion disks. This will also provide a basis for applying such MHD models to PMS disks of HeAeBe stars.

Acknowledgments

References

Alecian, E., Wade, G. A., Catala, C., *et al.* 2013a, *MNRAS*, 429, 1001
Alecian, E., Wade, G. A., Catala, C., *et al.* 2013b, *MNRAS*, 429, 1027
Babel J., & Montmerle T., 1997a, *ApJ*, 485, L29
Babel J. & Montmerle T., 1997b, *A&A*, 323, 121
Chlebowski T., Harnden Jr. F. R., & Sciortino S., 1989, *ApJ*, 341, 427
Gagné M., Oksala M. E., Cohen D. H., Tonnesen S. K., ud-Doula A., Owocki S. P., Townsend R. H. D., & MacFarlane J. J., 2005, *ApJ*, 628, 986
Grunhut, J. H., Wade, G. A., Leutenegger, M., *et al.* 2013, *MNRAS*, 428, 1686
Hillenbrand, L. A. 1997, *AJ*, 113, 1733
Kivelson, M. G. & Southwood, D. J., 2005, *Journal of Geophysical Research (Space Physics)*, **110**, 12209
Kochukhov, O., Lundin, A., Romanyuk, I., & Kudryavtsev, D. 2011, *ApJ*, 726, 24
Owocki S. P., Sundqvist J. O., Cohen D. H., & Gayley K. G., 2013, *MNRAS*, 429, 3379
Petit V., Owocki S. P., Wade G. A., Cohen D. H., Sundqvist J. O., Gagné M., Maíz Apellániz J., Oksala M. E., Bohlender D. A., Rivinius T., Henrichs H. F., Alecian E., Townsend R. H. D., ud-Doula A., & MiMeS Collaboration 2013, *MNRAS*, 429, 398
Sundqvist, J. O., ud-Doula, A., Owocki, S. P., Townsend, R. H. D., Howarth, I. D., & Wade, G. A., 2012, *MNRAS*, **423**, L21
Townsend, R. H. D., 2008, *MNRAS*, **389**, 559
Townsend, R. H. D., Oksala, M. E., Cohen, D. H., Owocki, S. P., & ud-Doula, A., 2010, *ApJ*, **714**, L318
Townsend, R. H. D. & Owocki, S. P., 2005, *MNRAS*, **357**, 251
Townsend, R. H. D., Owocki, S. P., & Groote, D., 2005, *ApJ*, **630**, L81
Townsend, R. H. D., Owocki, S. P., & ud-Doula, A., 2007, *MNRAS*, **382**, 139
ud-Doula A. & Owocki S. P., 2002, *ApJ*, 576, 413
ud-Doula A., Owocki S. P., & Townsend R. H. D., 2008, *MNRAS*, 385, 97
ud-Doula A., Owocki S. P., & Townsend R. H. D., 2009, *MNRAS*, 392, 1022
ud-Doula A., Sundqvist J. O., Owocki S. P., Petit V., & Townsend R. H. D., 2013, *MNRAS*, 428, 2723